Applied Catalysis B: Environmental 251 (2019) 87–93

Contents lists available at ScienceDirect

Applied Catalysis B: Environmental

journal homepage: www.elsevier.com/locate/apcatb

One-pot synthesis of porous 1T-phase MoS_2 integrated with single-atom Cu doping for enhancing electrocatalytic hydrogen evolution reaction

Liang Ji[a,1], Pengfei Yan[a,1], Chuanhui Zhu[a], Chunyan Ma[b], Wenzhuo Wu[a], Cong Wei[a], Yonglong Shen[a], Shengqi Chu[c], Jiaou Wang[c], Yi Du[d], Jun Chen[e], Xinan Yang[f], Qun Xu[a,*]

[a] College of Materials Science and Engineering, Zhengzhou University, Zhengzhou 450052, PR China
[b] Key Laboratory of Environmental Nanotechnology and Health Effects, Research Center for Eco-Environmental Sciences, Chinese Academy of Sciences, Beijing 100085, PR China
[c] Beijing Synchrotron Radiation Facility, Institute of High Energy Physics, Chinese Academy of Sciences, Beijing 100049, PR China
[d] Institute for Superconducting & Electronic Materials, Australian Institute of Innovative Materials, Innovation Campus, University of Wollongong, Northfields Avenue, Wollongong, NSW 2500, Australia
[e] Intelligent Polymer Research Institute, Australian Institute of Innovative Materials, Innovation Campus, University of Wollongong, Northfields Avenue, Wollongong, NSW 2500, Australia
[f] National Laboratory for Condensed Matter Physics and Institute of Physics, Chinese Academy of Sciences, Beijing 100190, PR China

ARTICLE INFO

Keywords:
Transition-metal dichalcogenides
One-pot synthesis
Atomic doping
Electrocatalyst
Hydrogen evolution reaction

ABSTRACT

Molybdenum sulfide (MoS_2) has attracted great interest as a promising non-precious-metal catalyst candidate to replace the precious-metal Pt catalysts for the hydrogen evolution reaction (HER). Nevertheless, the catalytic efficiency of MoS_2 is significantly restricted by its density of catalytic active sites and inert basal plane. In this work, we have designed a facile one-pot solvothermal method to synthesize porous 1T-MoS_2 that is integrated with atomic doping of Cu atoms. The as-prepared Cu@MoS_2 sample exhibits enhanced HER performance with a low overpotential of 131 mV at the current density of 10 mA/cm^2, a small Tafel slope of 51 mV/dec and as well as a good long-term stability. Enhanced HER performance can be ascribed to the synergistic effect of 1T-MoS_2 metallic phase, single atom Cu doping and numerous sulfur vacancies. Theoretical calculations indicates that the adsorption energy of Cu atom on 1T-MoS_2 surface (−3.68 eV) is much higher than that on 2H-MoS_2 surface (−1.94 eV), moreover, the Cu atom adsorbed on the surface of the 1T-MoS_2 has larger charge transfer (−0.38e), which can be contributed to further enhance HER performance of 1T-MoS_2.

1. Introduction

Hydrogen is considered as an ideal clean and sustainable energy source to overcome the unacceptable long-term consequences of fossil fuels. [1,2] It can be generated through coal gasification [3], biomass processing technologies [4], hydrolysis [5–9] etc. Among all the technologies, water electrolysis is one of the most efficient methods for hydrogen production [1,10]. So far, platinum (Pt) has been widely recognized as the most electroactive catalyst for the hydrogen evolution reaction ($2H^+ + e^- \rightarrow H_2$), but its high cost as a noble metal catalyst limits its large-scale application. Thus, how to find inexpensive earth-abundant materials as substitutes is urgent [11–14]. Two-dimensional transition metal dichalcogenides (TMDs) have opened up a promising path to this due to their earth-abundance, low-cost and outstanding catalytic abilities demonstrated by both theoretical calculations and experimental results [15–17].

Molybdenum sulfide is a typical kind of TMD, which has been widely studied as an electrocatalyst owing to its highly active catalytic edge sites [18]. The limited number of active sites and inert basal planes of MoS_2, however, dramatically restrict its catalytic efficiency in the HER [15,16]. Intensive efforts have been devoted to narrowing the gap between MoS_2 and Pt based catalysts. One widely recognized strategy is transforming the semiconducting 2H-MoS_2 to metallic 1 T-MoS_2 through phase engineering, which will make the basal plane catalytically available, thus dramatically enhancing the catalytic capability of MoS_2 [19,20]. In addition, improving the density of active edge sites also can be achieved by introducing sulfur vacancies or making the structure porous [21,22]. What is more, doping exotic elements (Zn, Co, Pd) into it can influence the electron density of MoS_2 through electron transfer between the dopants and MoS_2, which will

* Corresponding author.
E-mail address: qunxu@zzu.edu.cn (Q. Xu).
[1] These authors contributed equally.

https://doi.org/10.1016/j.apcatb.2019.03.053
Received 3 January 2019; Received in revised form 15 March 2019; Accepted 18 March 2019
Available online 23 March 2019
0926-3373/

boost its HER performance [23,24]. Nevertheless, finding how to simultaneously achieve the above strategies in one material system, *i.e.*, transforming 2H-MoS_2 to porous metallic 1T-MoS_2, introducing sulfur vacancies, and doping exotic elements into MoS_2, is challenging.

Herein, we report a facile one-pot solvothermal synthesis of porous 1 T-phase MoS_2, which simultaneously possesses sulfur vacancies and features atomic doping of Cu atoms. The synthesized Cu@MoS_2 exhibits outstanding electrocatalytic performance toward the HER with a small overpotential of 131 mV for an areal current density of 10 mA/cm^2, a Tafel slope of 51 mV/dec, and long term stability. In the as-prepared Cu@MoS_2, the porous structure and 1 T-MoS_2 can simultaneously activate the basal plane and supply more active edge sites, the doping Cu atoms can lead to electron transfer between Cu and MoS_2. More importantly, we apply the first principles calculation and it demonstrates that the stronger stability and larger charge transfer under the condition of Cu adsorbing on 1 T-MoS_2 surface other than on 2H-MoS_2. So it reveals that the metastable 1 T-MoS_2 monolayer offers potential advantages over 2H-MoS_2 in the adsorption of single metal atom to help enhancing HER performance.

2. Experimental section

2.1. Material

MoO_3 powder with the representative lateral size was purchased from Alfa Aesar (product number 011873). Thioacetamide, cupric nitrate, N, N-Dimethylformamide (DMF) and ethanol used in following experiments were all purchased from Sinopharm Chemical Reagent Co., Ltd. (China). Commercial Pt/C (20% Pt) was purchased from Johnson Matthey. All of the reagents mentioned above were used without further purification. Aqueous solution was prepared with double-distilled water.

2.2. Synthesis of Cu@MoS_2 and pristine MoS_2

30 mg MoO_3, 45 mg thioacetamide, 53.2 mg urea and 10 mg Cu $(NO_3)_2$ were dissolved in 30 ml N, N-Dimethylformamide (DMF) and sonicated for 2 h to achieve a homogenous solution. Then the solution was transferred into a Teflon-lined autoclave and loaded into an oven maintaining at 200°C for 20 h. Next the autoclave was removed from the oven and cooled to the room temperature naturally. Finally, the product was washed several times with ethanol and then centrifuged at 8000 rpm for 10 min, followed by drying in a furnace at 40 °C. For comparison, Cu@MoS_2 with different mass ratios of Cu (1.17%, 2.21%, 3.6%, 3.4%) can be synthesized by controlling the weight of $Cu(NO_3)_2$ (5, 10, 25, and 50 mg). The same procedure was used to prepare pristine MoS_2 as the control experiment except for adding of $Cu(NO_3)_2$ precursor.

2.3. Characterization

The morphology and microstructure of the samples were analyzed by using Field-emission SEM (JSM7500 F) and TEM (JEM-2100). The high-angle annular dark-filed (HAADF) STEM images and elemental mapping were taken by using FEI Tecnai G2F20 S-TWIN microscope operated at 200 kV. The Raman spectroscopy was carried out on a LabRAM HR Evolution with laser wavelength of 532 nm. The XRD patterns of the samples were tested by Y-2000 X-ray Diffractometer with copper Kαradiation (λ = 1.5406 Å). XPS spectra was achieved on ESCLAB 280 system with Al/K (photon energy = 1486.6 eV) anode mono X-ray source. Extended X-ray absorption fine structure (EXAFS) spectra was obtained by using 1W1B-XAFS experiment station of the Beijing Synchrotron Radiation Facility (BSRF). The H_2 gas evolution rate was measured with a gas chromatograph (SP-7820) at the current density of 10 mA/cm^2 in an H-type three-electrode electrochemical cell (Ag/AgCl reference electrode and a Pt plate counter electrode) with 0.5 M H_2SO_4.

2.4. Electrochemical measurements

An electrochemical station (CHI660D) with a three-electrode system was used to achieve all the electrochemical measurements. For preparing the working electrode, 1 mg samples (Cu@MoS_2, MoS_2 and Pt/C) and 5 μL 5 wt% nafion solution were dispersed in 1 ml ethanol with 30 min batH–Sonication to form a homogenous solution, then 20 μL of the solution was deposited on a glassy carbon electrode. The loading weight of different samples (Cu@MoS_2, MoS_2 and Pt/C) on electrode was 0.02 mg, and the area of the electrode was 0.196 cm^2. Ag/AgCl and graphite rod were used as the reference electrode and the counter electrode, respectively. All of the measurements were performed in N_2-saturated 0.5 mol/L H_2SO_4 electrolyte. Linear sweep voltammetrys (LSVs) was performed at a scan rate of 25 mV/s. The chronoamperometry measurements of HER were carried out at the current density of 10 mA/cm^2.

TOF values were calculated using the following equation

$$\mathrm{TOF}\ (s^{-1}) = (j*A)/(2*F*n)$$

In the equation, j (mA/cm^2) is the current density at a specific overpotential, A (cm^2) is the surface area of the electrocatalyst, 2 indicates that 1 mole of H_2 was generated by 2 electrons, F is 96485.3 (C/mol) which is Faraday's constant, and n means the moles of electrocatalysts loading on the electrode.

The electrochemically active surface areas (ECSA) can be calculated according to the equation ECSA = $R_f S$, in which S is the surface area of the electrode. Rf is directly proportional to the double layer capacitance (C_{dl}), which can be measured by cyclic voltammetry measurement in different scan rates (such as 20, 40, 60, 80, 100 mV/s) within the potential windows of −0.25˜ −0.35 V *vs*. RHE.

2.5. Computational details

The first-principles calculations based on density functional theory in the CASTEP plane-wave pseudopotential package with Perdew-Burke-Ernzerhof exchange-correlation function were performed [25,26]. For the supercells containing 16 Mo atoms and 32 S atoms, the cutoff energy of the plane-wave basis was 421.8 eV, 2*2*1 k-points meshes were used for the Brillouin zone sampling [27], but as for the pristine unit cells, 8*8*5 k-points meshes were set to ensure the accuracy of the calculation results. Simultaneously, the electron-ion interactions were described by the ultrasoft pseudopotentials (USPPs) [28], and the self-consistent field (SCF) calculation was kept within the energy convergence criterion of 1×10^{-6} eV/atom, and the DFT-D was used for dispersion corrections [29].

As shown in Fig. S1, the structures of the 1 T-MoS_2 (4 × 4) and 2H-MoS_2 (4 × 4) were optimized by using the BroydenFletcher-Goldfarb-Shanno (BFGS) minimization scheme [30]. In addition, the surfaces of the 1 T-MoS_2 and 2H-MoS_2 were simulated using a three-dimensional (3D) periodic slab model, the distance between two adjacent monolayers was larger than 20 Å to avoid the layer–layer interaction. The total energy was converged within 1×10^{-5} eV/atom, and the maximum force was converged within 0.03 eV/Å, while the maximum stress was converged within 0.05 GPa, and the maximum atom displacement was converged within 0.001 Å.

The adsorption energy (E_{ads}) of Cu atom in the adsorbed system is defined as

$$E_{ads} = E_{Cu+MoS_2} - E_{Cu} - E_{MoS_2}$$

Where E_{Cu+MoS_2} and E_{MoS_2} are the total energies of the monolayer with and without Cu, E_{Cu} is the energy of the free Cu atom. By definition, more negative adsorption energy suggests a more favorable exothermic Cu adsorption on the MoS_2 surface.

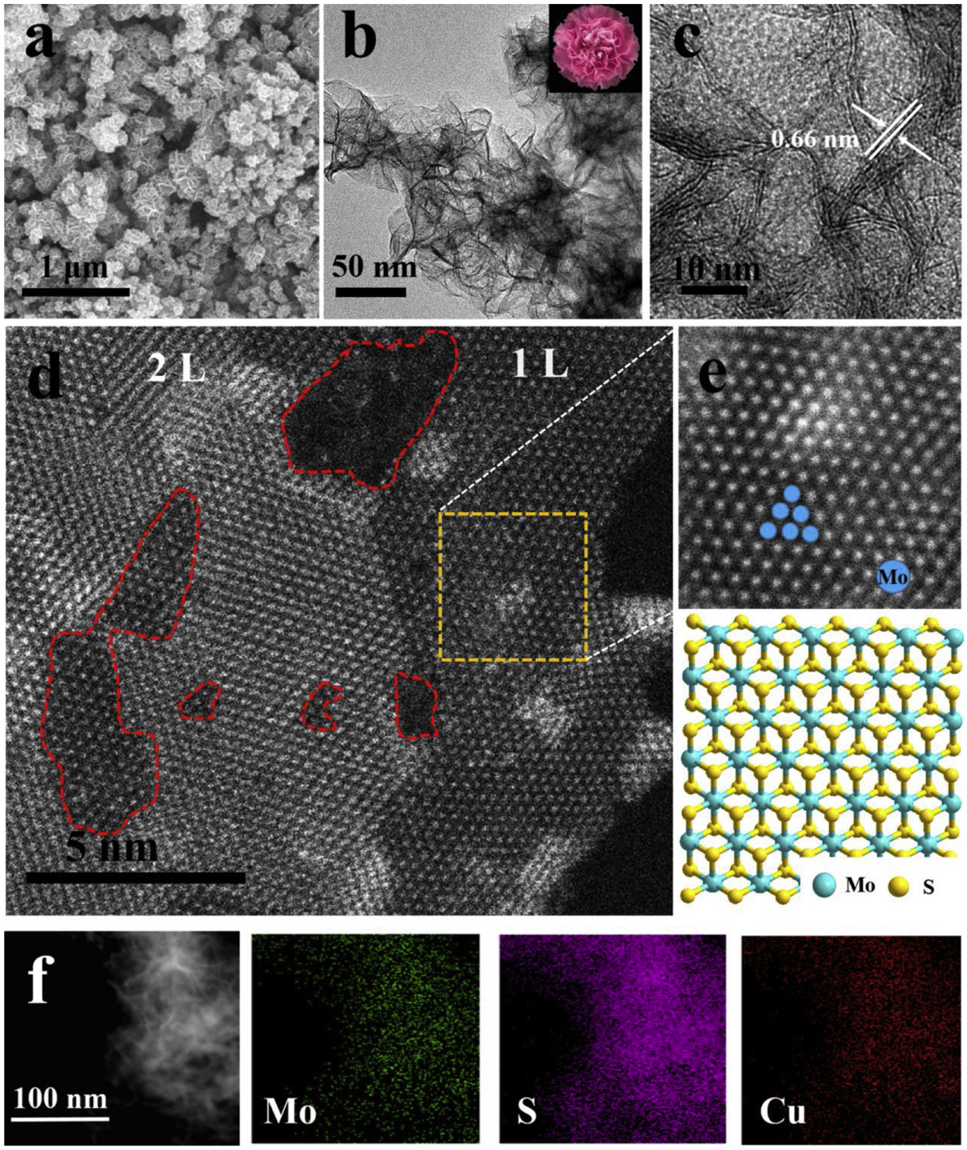

Fig. 1. Morphological characterizations of the catalysts. (a) SEM image of Cu@MoS_2. (b) TEM image of Cu@MoS_2. (c) HRTEM image of Cu@MoS_2. (d) HAADF-STEM image of Cu@MoS_2, which shows the ultrathin structure consisting of 1 or 2 layers. The defects are circled by the red dotted lines. (e) Filtered image of the orange square in (d). (f) Element mapping images of Mo, S, and Cu in Cu@MoS_2 (For interpretation of the references to colour in this figure legend, the reader is referred to the web version of this article).

3. Results and discussion

Scanning electron microscope (SEM) and transmission electron microscope (TEM) images of the as-prepared Cu@MoS_2 nanosheets are shown in Fig. 1a and b. It can be observed the morphologies are flowerlike in the SEM and TEM images. To further verify the structure of the nanosheets, a high-resolution TEM (HRTEM) image is shown in Fig. 1c, where a few-layer structure with a layer spacing of 0.66 nm can be observed, a value which can be ascribed to the (002) crystalline planes of MoS_2 [24]. Furthermore, the detailed atomic-resolution structure was further characterized by high-angle annular dark field – scanning transmission electron microscopy (HAADF-STEM), as shown in Fig. 1d and Fig. S2 in the Supporting Information. It can be observed that the ultrathin few-layer nanosheets are composed of only 1 or 2 layers with numerous S-vacancies and variable size pore. Besides the vacancies and porous structure, the typical orthorhombic structure of 1 T-MoS_2 can be seen in Fig. 1e. And it can be found that no clusters or nanoparticles can be found, which could exclude the possibility of forming the copper clusters on the surface of MoS_2. The STEM characterization is consistent with the energy dispersive X-ray spectroscopy (EDX) mapping results (Fig. 1f), which shows the homogenous element distributions of Mo (green color), S (purple color), and Cu (red color).

The characterization above indicates that the introduction of Cu cannot significantly change the morphology of MoS_2, but it has an apparent effect on its size and lateral thickness. In the control experiment without using $Cu(NO_3)_2$ as the precursor in the reaction, the size of the synthesized pristine MoS_2 is around 500 nm (Fig. S3), is nearly 5 times the size of the Cu@MoS_2 (100 nm). So the introduction of Cu can help to decrease the size of MoS_2, and it can lead to an increase in the specific surface area successfully. It is well-known that a larger specific surface area can contribute to the higher catalytic performance. Different amounts of $Cu(NO_3)_2$ precursor were used to compare the as-prepared catalyst, and it was found that the Cu@MoS_2 would have an optimal morphology in terms of size and thickness when the added amount was 10 mg (Fig. S4) compared to 5 mg (Fig. S5), and 50 mg (Fig. S6).

X-ray photoelectron spectroscopy was used to investigate the

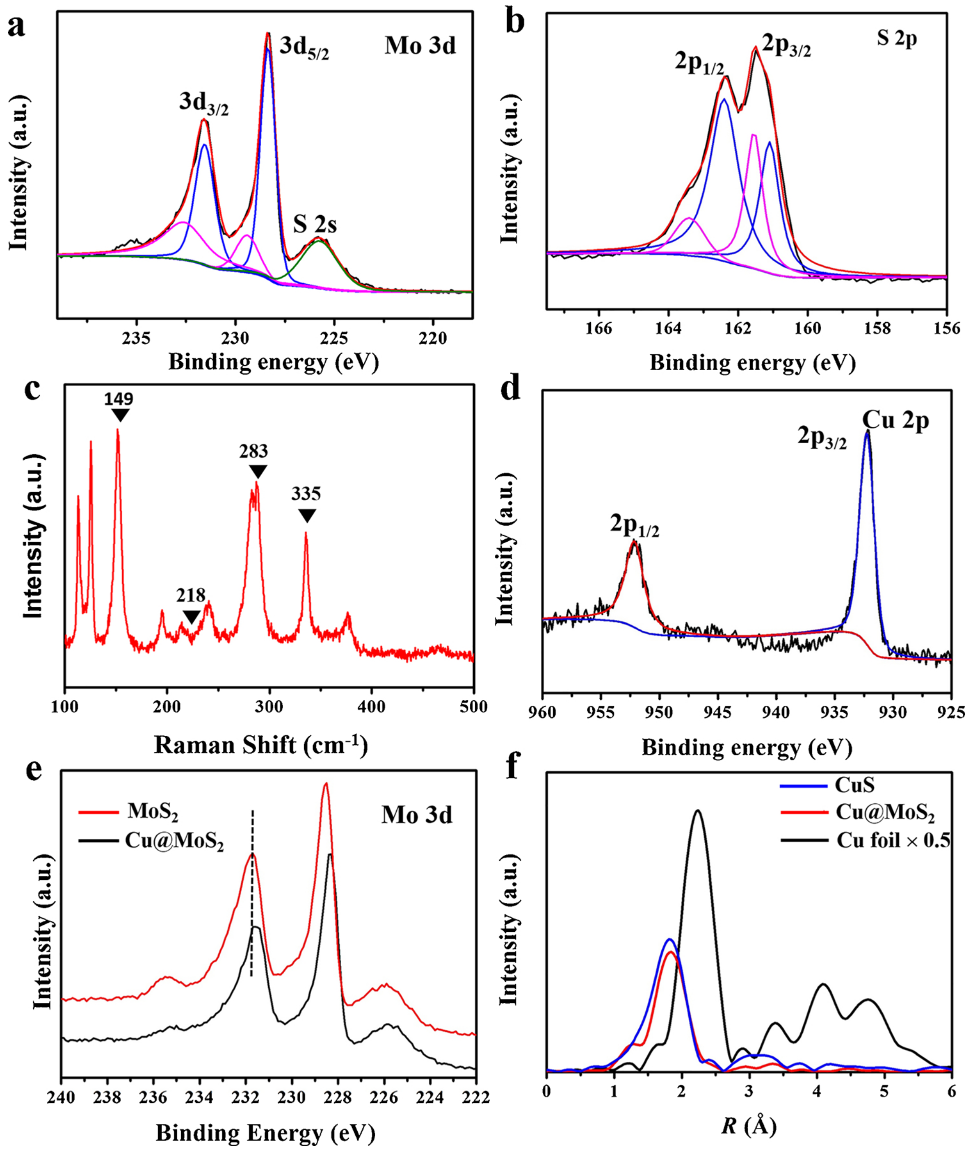

Fig. 2. Spectral characterization of the catalysts. (a, b) High-resolution X-ray photoelectron spectroscopy (XPS) spectra of Mo 3d (a) and S 2p (b). (c) Raman spectra of $Cu@MoS_2$. (d) XPS spectra of Cu 2p. (e) XPS spectra of Mo 3d for $Cu@MoS_2$ and pristine MoS_2. (f) Cu K^2-weighted Fourier transform spectra of $Cu@MoS_2$, CuS, and Cu foil.

element states and confirm the combination of Cu and MoS_2. As shown in Fig. 2a, the Mo 3d spectrum consists of two peaks for $3d_{5/2}$ and $3d_{3/2}$ located at 228.4 and 231.6 eV, respectively, which can be ascribed to the Mo^{4+} in metallic 1 T-MoS_2. The peaks located at around 229.4 and 232.6 eV can be attributed to the 2H-MoS_2, which are about 1 eV higher than the corresponding peaks in 1 T-MoS_2 [31,32]. The S 2p peaks locating at 161.1 eV and 162.4 eV in Fig. 2b can be ascribed to the $2p_{3/2}$ and $2p_{1/2}$ orbitals of S^{2-} in 1 T-MoS_2 [32]. This characterization result therefore further indicates the existence of 1 T-MoS_2, which is in agreement with the Raman spectra in Fig. 2c. The Raman peaks at 149, 218, 283, and 335 cm^{-1} are ascribed to the phonon modes of 1 T-MoS_2 [33–35]. The Cu $2p_{3/2}$ and $2p_{1/2}$ peaks located at 932.3 eV and 952.2 eV in Fig. 2d also confirm the presence of Cu in MoS_2 [36]. Furthermore as shown in Fig. 2e, the intense electronic interaction between Cu and MoS_2 induces the Mo peaks a negative shift of about 0.22 eV compared with the pristine MoS_2, which indicates the increasing surface electron density of MoS_2 because of Cu doping. The electron rich MoS_2 will weaken the H–S bonds and facilitate the release of H atoms adsorbed on the MoS_2, so that the HER process will be enhanced by the optimization of the hydrogen adsorption energy [24,37–39]. To study the bonding environment of Cu atoms, extended X-ray absorption fine structure (EXAFS) spectra were collected, and the Fourier transform of the K^2-weighted Cu K-edge EXAFS spectrum indicates that there is only one peak located at 1.8 Å, corresponding to the Cu-S band, and no appreciable Cu-Cu peak was observed in $Cu@MoS_2$, which indicates the absence of Cu clusters, and Cu atoms are atomically dispersed in the as-prepared $Cu@MoS_2$.

The morphology and structural characterization above indicate that $Cu@MoS_2$ has been successfully synthesized. The typical synthesis procedure is shown in Fig. S8. The detailed reaction mechanism was further studied through a series of control experiments that involved adjusting the amount of precursor $Cu(NO_3)_2$. In our experimental design, MoO_3 is an ideal candidate for the starting material because of its octahedral structure same with that of the intended product of 1 T-MoS_2. Thioacetamide was chosen as the sulfur source, and urea was chosen as the weak reducer to obtain MoS_2. Furthermore, $Cu(NO_3)_2$ was chosen as the reactant to obtain the hetero-atom Cu doped on MoS_2. The experimental results indicate that $Cu(NO_3)_2$ plays a key role in the reaction. As shown in Fig. S7a, a new peak locating at 235.5 eV appeared when the amount of $Cu(NO_3)_2$ was increased to 50 mg, which is

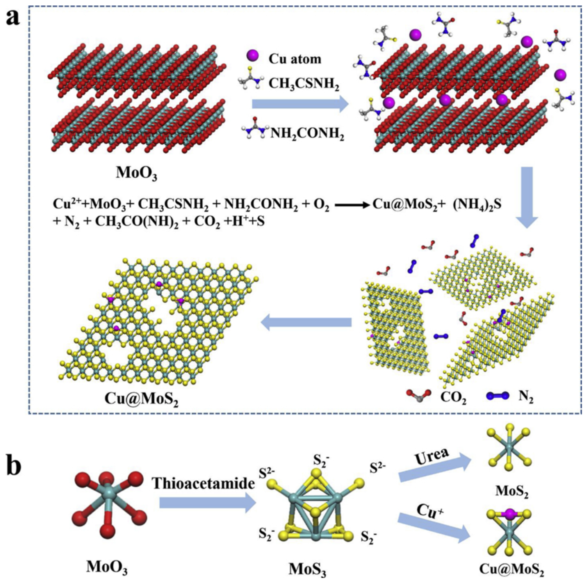

Fig. 3. Schematic illustration of the formation mechanism of Cu@MoS_2.

ascribed to the unreduced Mo^{6+} in MoO_3. This phenomenon can supply an important clue that thioacetamide first reacts with $Cu(NO_3)_2$, and then it sulfurizes the MoO_3 to MoS_3. During the process, Cu^{2+} will be reduced to Cu^+ in the presence of thioacetamide, which can be demonstrated in Fig. S7b. With the increasing amount of $Cu(NO_3)_2$, the binding energies of Cu $2p_{3/2}$ and $2p_{1/2}$ are slightly shifted to 931.8 and 951.8 eV, which indicates the presence of Cu^+ [40]. If the amount of Cu $(NO_3)_2$ is too large, more thioacetamide will be consumed, leading to the presence unsulfurized MoO_3 and thus inhibiting the following reduction process.

In the subsequent step, on the one hand, once MoO_3 was sulfurized by thioacetamide to produce MoS_3, the latter can be subsequently reduced by weak reducing agents to metallic phase MoS_2 [32,41–43]. As shown in Fig. 3b, the lattice of MoS_3 can transform to metallic MoS_2 after the S_2^- edge bonds are reduced by urea (MoS_3 + NH_2CONH_2 + O_2 → MoS_2 + N_2 + CO_2 + H_2O) and Cu^+ (Cu^+ + MoS_3 → Cu@MoS_2 + Cu^{2+} + S). At the same time, the obtained MoS_2 would keep evolving to form the layered structure. The reduction of MoS_3 can be further authenticated by the XRD patterns shown in Fig. S9. A strong peak locating at 22.8° is a typical (101) plane reflection of sulfur crystal, which indicates the successful reduction of MoS_3. On the other hand, after the oxidization-reduction process, Cu atoms can insert themselves in the S layer and bond with sulfur atoms, as shown in Fig. 3b. In addition, it is worthwhile to note that the generation of the N_2 and CO_2 will not only benefit the exfoliation of MoS_2, but also benefit the formation of porous structured MoS_2 as shown in Fig. 1d and S2.

The polarization curves of Cu@MoS_2 and the control samples of pristine MoS_2 and Pt/C are shown in Fig. 4a. Cu@MoS_2 shows higher current densities than pristine MoS_2 (e.g., at −0.2 and −0.15 V), and the overpotential of Cu@MoS_2 (black line) is only 131 mV when the current density is 10 mA/cm^2, which is smaller than that of pristine MoS_2 (red line), and just behind the Pt/C (blue line). In addition, the tafel slop of Cu@MoS_2 (51 mV/dec) is also much smaller than that of pristine MoS_2 (95 mV/dec) as illustrated in Fig. 4b. These values suggest that the doping of Cu dramatically enhanced the HER activity of MoS_2, making Cu@MoS_2 a comparable or even better catalytic performer than many state-of-the-art catalysts reported in the literature, as shown in Table S1. The electrochemical activity of Cu@MoS_2 is dramatically influenced by the precursor mass of $Cu(NO_3)_2$ as shown in the volcano-shaped plot in Fig. 4c and Fig. S10, which demonstrate that only appropriate mass of $Cu(NO_3)_2$ precursor can lead to the best catalytic ability. We speculated such a phenomenon is caused by the fact that unreduced MoO_3 will weaken the HER performance due to its poor conductivity. In our reaction, increasing the amount of $Cu(NO_3)_2$ precursor will improve the Cu mass ratio. However, when the usage of Cu $(NO_3)_2$ is too large, it will consume too much thioacetamide and suppress the sulfurization process of MoO_3 thus lead to the unreduced MoO_3. Electrochemical surface areas (ECSA) can be represented by measuring the double-layer capacitance (C_{dl}) using a cyclic voltammetry method (Fig. S11) [44], and S12 a shows that the ECSA of Cu@MoS_2 is much larger than those of MoS_2. The turnover frequency (TOF) values of Cu@MoS_2, MoS_2 and Pt/C were measured at different overpotentials as shown in Fig. S12b, Cu@MoS_2 features much larger TOF values than that of MoS_2 at different overpotentials, which has narrowed the gap with Pt/C. To estimate the long-term stability of the catalysts, the chronoamperometry measurements of HER were carried out at the current density of 10 mA/cm^2. As shown in Fig. 4d, Cu@MoS_2 owns the splendid long term stability which is nearly unchangeable compared with Pt/C (Fig. S12c) and MoS_2. The H_2 gas evolution rate of Cu@MoS_2 at the current density of 10 mA/cm^2 was measured by gas chromatograph as shown in Fig. S13, which shows an average rate of 7.51 mLg^{-1} cm^{-2} min^{-1}. In a word, the doping of Cu atoms into MoS_2 made Cu@MoS_2 more favorable catalytic abilities comparing with pristine MoS_2, which can be attributed to the larger TOF and ECSA values, and a dependable long-term durability.

To understand the perfect catalytic performance of Cu@MoS_2, the different adsorption energy and electron transfer of Cu adsorption on the surface of 1 T-MoS_2 and 2H-MoS_2 has been calculated and investigated. Two typical adsorption positions of 2H-MoS_2 were tested and at the same time, considering the instability of 1 T-MoS_2, four adsorption positions of the Cu atom on the 1 T-MoS_2 monolayer was examined (Fig. 5). All structures were fully relaxed to ensure the accuracy of the calculation results, the lattice constants of the optimized pristine unit cells of the 1 T-MoS_2 and 2H-MoS_2 are a = b = 3.198 Å, c = 5.651 Å, and a = b = 3.161 Å, c = 12.143 Å, respectively, which are similar to others reports: 1 T-MoS_2 crystallizes in the space group P3m1 with a cell of a = b = 3.190 Å and c = 5.945 Å, [45] the lattice constant of 2H-MoS_2 is a = b = 3.140 Å, c = 12.530 Å (JCPDS 75–1539). As shown in Fig. 5, Cu atom is adsorbed on the plane of S atoms, and there are three adjacent S atoms. The adsorption energies of Cu atom adsorbed on the 2H-MoS_2 are −1.67 and −1.94 eV, meanwhile the adsorption energies of Cu adsorbed on the 1 T-MoS_2 is in the range from −2.87 to −3.68 eV (Table S2), the more negative adsorption energy suggests the Cu adsorption configuration on 1 T-MoS_2 is more stable than that on 2H-MoS_2. And this conclusion can be confirmed again from the different bond lengths between Cu and the adjacent S atoms in various Cu adsorption configurations (Table S3), which indicates the bond lengths of the Cu adsorption configuration on 1 T-MoS_2 surface are much shorter than that in the Cu adsorption on 2H-MoS_2 surface.

In addition, Hirshfeld charge analysis demonstrates that the Cu atom adsorbed on 1 T-MoS_2 has the larger charge transfer, and the value on 2H-MoS_2 surface are −0.19 and −0.18 e. As a comparison, the charge transfer on 1 T-MoS_2 surface is in the range from −0.27 to −0.38 e (Table S2). The more negative charge transfer indicates that more electrons transferred from Cu to 1 T-MoS_2 after adsorption, and it means the electron-rich MoS_2 will weaken the H–S bonds to help facilitate the release of H atoms adsorbed on the MoS_2.

4. Conclusions

In summary, for the first time, porous 1 T-MoS_2 integrated with atomic doping of Cu atoms have been successfully synthesized via a facile one-pot solvothermal synthesis method. Our experimental results demonstrate this material system can enhance the catalytic performance toward HER efficiently. By tuning the ratio of precursor of Cu (NO3)$_2$, the micromorphology, porous structure, and density of the active sites can be synergistically controlled. At suitable Cu atomic

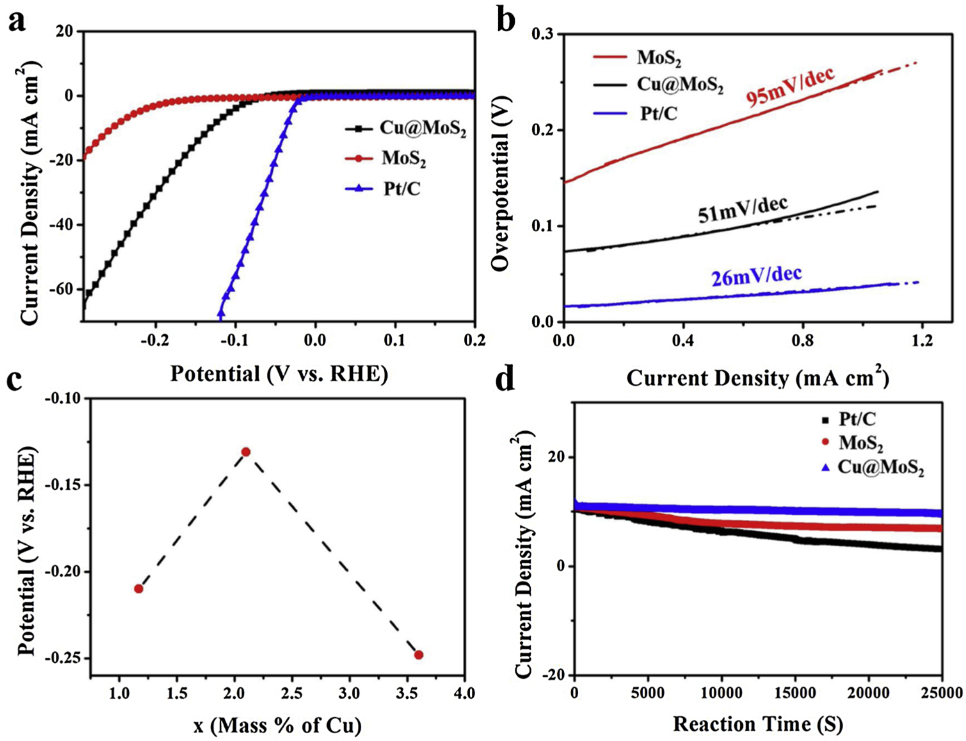

Fig. 4. Electrochemical activities of the catalyst toward HER. (a) Polarization curves of HER for Cu@MoS_2, Pt/C and MoS_2. (b) Tafel plots of Cu@MoS_2, Pt/C and pristine MoS_2. (c) Volcano-shaped plot of overpotentials at 10 mA/cm^2 of Cu@MoS_2 with different $Cu(NO_3)_2$ precursor mass. (d) Chronoamperometry measurements of Pt/C, pristine MoS_2 and Cu@MoS_2 at the current density of 10 mA/cm^2.

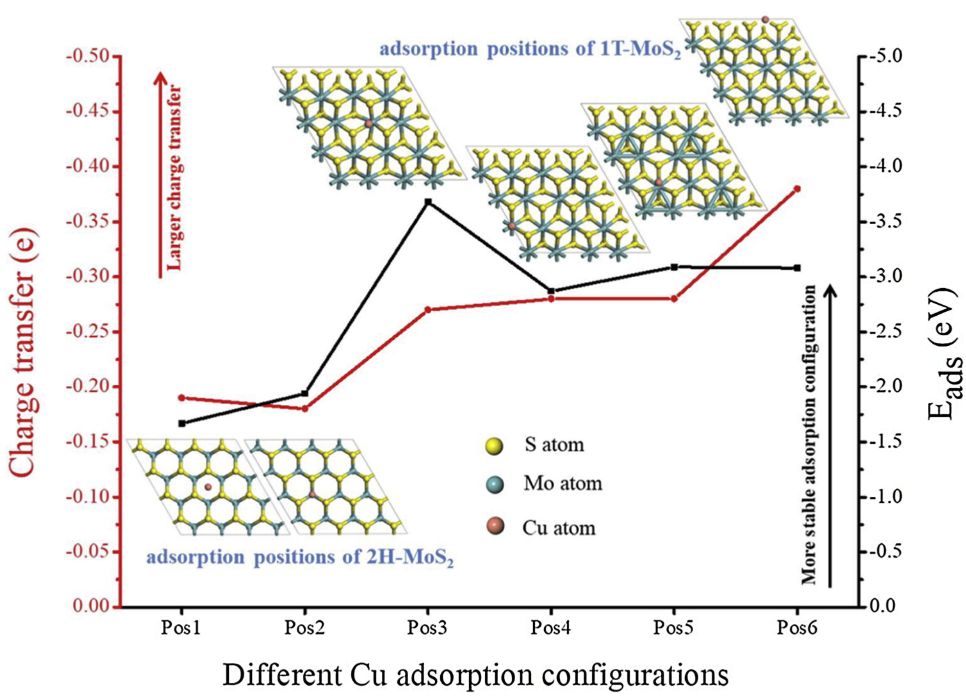

Fig. 5. The different adsorption energy, bond lengths between Cu and the adjacent S atoms and electron transfer of Cu adsorption on the surface of 1 T-MoS_2 and 2H-MoS_2. Cu atom adsorbed on the surface of the 2H-MoS_2. Above the center of the hexatomic ring (Pos1) and on the top site of a Mo atom (Pos2). Cu atom adsorbed on the surface of the 1 T-MoS_2, on the top site of the bridge site between a Mo-S bond (Pos3 and Pos5) and on the top site of a Mo atom (Pos4 and Pos6).

doping, the as-synthesized Cu@MoS_2 exhibits superior electrocatalytic activity with a low overpotential of 131 mV at 10 mA/cm^2, Tafel slope of 51 mV/dec and a good long-term durability. DFT calculations indicates that Cu doping not only stabilize 1 T-MoS_2, but also can help to enhance the charge transfer of MoS_2 to improve the HER activity efficiently. Therefore this study has enriched the family of non-precious-metal catalysts, and it paves the way to a promising future in renewable clean energy in the future.

Acknowledgements

We are grateful to the National Natural Science Foundation of China (No. 21773216, 51173170, 21571157), the financial support from the Innovation Talents Award of Henan Province (114200510019), the Program of science and technology (182102410073) from Henan Province, and the support of Gongji Chen and Runjie Liu from Supercomputing Center in Zhengzhou University, the Center for modern analysis and computation of Zhengzhou University, the Australian Research Council (CE 140100012 and DP170102267) and as

well as the Australian National Fabrication Facility – Materials node and UOW Electron Microscopy Centre for equipment use.

Appendix A. Supplementary data

Supplementary material related to this article can be found, in the online version, at doi:https://doi.org/10.1016/j.apcatb.2019.03.053.

References

[1] J.A. Turner, Sustainable hydrogen production, Science 305 (2004) 972–974.
[2] M.S. Dresselhaus, I.L. Thomas, Alternative energy technologies, Nature 414 (2001) 332–337.
[3] G.J. Stiegel, M. Ramezan, Hydrogen from coal gasification: an economical pathway to a sustainable energy future, Int. J. Coal Geol. 65 (2006) 173–190.
[4] M. Ni, D.Y.C. Leung, M.K.H. Leung, K. Sumathy, An overview of hydrogen production from biomass, Fuel Process. Technol. 87 (2006) 461–472.
[5] M. Huang, L. Ouyang, Z. Chen, C. Peng, X. Zhu, M. Zhu, Hydrogen production via hydrolysis of Mg-oxide composites, Int. J. Hydrogen Energy 42 (2017) 22305–22311.
[6] M. Huang, L. Ouyang, H. Wang, J. Liu, M. Zhu, Hydrogen generation by hydrolysis of MgH_2 and enhanced kinetics performance of ammonium chloride introducing, Int. J. Hydrogen Energy 40 (2015) 6145–6150.
[7] M. Ma, R. Duan, L. Ouyang, X. Zhu, C. Peng, M. Zhu, Hydrogen generation via hydrolysis of H-$CaMg_2$ and H-$CaMg_{1.9}Ni_{0.1}$, Int. J. Hydrogen Energy 42 (2017) 22312–22317.
[8] M. Ma, R. Duan, L. Ouyang, X. Zhu, Z. Chen, C. Peng, M. Zhu, Hydrogen storage and hydrogen generation properties of $CaMg_2$ -based alloys, J. Alloys. Compd. 691 (2017) 929–935.
[9] L. Ouyang, W. Chen, J. Liu, M. Felderhoff, H. Wang, M. Zhu, Enhancing the regeneration process of consumed $NaBH_4$ for hydrogen storage, Adv. Energy Mater. 7 (2017) 1700299.
[10] J. Deng, H. Li, J. Xiao, Y. Tu, D. Deng, H. Yang, H. Tian, J. Li, P. Ren, X. Bao, Triggering the electrocatalytic hydrogen evolution activity of the inert two-dimensional MoS_2 surface via single-atom metal doping, Energy Environ. Sci. 8 (2015) 1594–1601.
[11] H. Wang, L.Y. Ouyang, G.F. Zou, C. Sun, J. Hu, X. Xiao, L.J. Gao, Optimizing MoS_2 edges by alloying isovalent W for robust hydrogen evolution activity, ACS Catal. 8 (2018) 9529–9536.
[12] X. Huang, M. Leng, W. Xiao, M. Li, J. Ding, T.L. Tan, W.S.V. Lee, J. Xue, Activating basal planes and S-terminated edges of MoS_2 toward more efficient hydrogen evolution, Adv. Funct. Mater. 27 (2017) 1604943.
[13] S. Chu, Y. Cui, N. Liu, The path towards sustainable energy, Nat. Mater. 16 (2016) 16–22.
[14] D. Voiry, H. Yamaguchi, J. Li, R. Silva, D.C. Alves, T. Fujita, M. Chen, T. Asefa, V.B. Shenoy, G. Eda, M. Chhowalla, Enhanced catalytic activity in strained chemically exfoliated WS_2 nanosheets for hydrogen evolution, Nat. Mater. 12 (2013) 850–855.
[15] M. Chhowalla, H.S. Shin, G. Eda, L.J. Li, K.P. Loh, H. Zhang, The chemistry of two-dimensional layered transition metal dichalcogenide nanosheets, Nat. Chem. 5 (2013) 263–275.
[16] J. Greeley, T.F. Jaramillo, J. Bonde, I.B. Chorkendorff, J.K. Norskov, Computational high-throughput screening of electrocatalytic materials for hydrogen evolution, Nat. Mater. 5 (2006) 909–913.
[17] H. Zhang, Ultrathin two-dimensional nanomaterials, ACS Nano 9 (2015) 9451–9469.
[18] D. Kiriya, P. Lobaccaro, H.Y. Nyein, P. Taheri, M. Hettick, H. Shiraki, C.M. Sutter-Fella, P. Zhao, W. Gao, R. Maboudian, J.W. Ager, A. Javey, General thermal texturization process of MoS_2 for efficient electrocatalytic hydrogen evolution reaction, Nano Lett. 16 (2016) 4047–4053.
[19] D. Voiry, A. Mohite, M. Chhowalla, Phase engineering of transition metal dichalcogenides, Chem. Soc. Rev. 44 (2015) 2702–2712.
[20] M.A. Lukowski, A.S. Daniel, F. Meng, A. Forticaux, L. Li, S. Jin, Enhanced hydrogen evolution catalysis from chemically exfoliated metallic MoS_2 nanosheets, J. Am. Chem. Soc. 135 (2013) 10274–10277.
[21] H. Li, C. Tsai, A.L. Koh, L. Cai, A.W. Contryman, A.H. Fragapane, J. Zhao, H.S. Han, H.C. Manoharan, F. Abild-Pedersen, J.K. Norskov, X. Zheng, Activating and optimizing MoS_2 basal planes for hydrogen evolution through the formation of strained sulphur vacancies, Nat. Mater. 15 (2016) 48–53.
[22] Y. Yin, J. Han, Y. Zhang, X. Zhang, P. Xu, Q. Yuan, L. Samad, X. Wang, Y. Wang, Z. Zhang, P. Zhang, X. Cao, B. Song, S. Jin, Contributions of phase, sulfur vacancies, and edges to the hydrogen evolution reaction catalytic activity of porous molybdenum disulfide nanosheets, J. Am. Chem. Soc. 138 (2016) 7965–7972.
[23] Z. Luo, Y. Ouyang, H. Zhang, M. Xiao, J. Ge, Z. Jiang, J. Wang, D. Tang, X. Cao, C. Liu, W. Xing, Chemically activating MoS_2 via spontaneous atomic palladium interfacial doping towards efficient hydrogen evolution, Nat. Commun. 9 (2018) 2120.
[24] Y. Shi, Y. Zhou, D.R. Yang, W.X. Xu, C. Wang, F.B. Wang, J.J. Xu, X.H. Xia, H.Y. Chen, Energy level engineering of MoS_2 by transition-metal doping for accelerating hydrogen evolution reaction, J. Am. Chem. Soc. 139 (2017) 15479–15485.
[25] S.J. Clark, M.D. Segall, C.J. Pickard, P.J. Hasnip, M.J. Probert, K. Refson, M.C. Payne, First principles methods using CASTEP, Z. Kristall. 220 (2005) 567–570.
[26] J.P. Perdew, K. Burke, M. Ernzerhof, Generalized gradient approximation made simple, Phys. Rev. Lett. 77 (1996) 3865–3868.
[27] H.J. Monkhorst, J.D. Pack, Special points for Brillouin-zone integrations, Phys. Rev. B Solid State (USA) 13 (1976) 5188–5192.
[28] D. Vanderbilt, Soft self-consistent pseudopotentials in a generalized eigenvalue formalism, Phys. Rev. B Condens. Matter (USA) 41 (1990) 7892–7895.
[29] F. Ortmann, F. Bechstedt, W.G. Schmidt, Semiempirical van der Waals correction to the density functional description of solids and molecular structures, Phys. Rev. B 73 (2006) 10.
[30] B.G. Pfrommer, M. Cote, S.G. Louie, M.L. Cohen, Relaxation of crystals with the quasi-Newton method, J. Comput. Phys. (USA) 131 (1997) 233–240.
[31] R. Kappera, D. Voiry, S.E. Yalcin, B. Branch, G. Gupta, A.D. Mohite, M. Chhowalla, Phase-engineered low-resistance contacts for ultrathin MoS_2 transistors, Nat. Mater. 13 (2014) 1128–1134.
[32] X. Geng, W. Sun, W. Wu, B. Chen, A. Al-Hilo, M. Benamara, H. Zhu, F. Watanabe, J. Cui, T.P. Chen, Pure and stable metallic phase molybdenum disulfide nanosheets for hydrogen evolution reaction, Nat. Commun. 7 (2016) 10672.
[33] Q. Liu, X. Li, Q. He, A. Khalil, D. Liu, T. Xiang, X. Wu, L. Song, Gram-scale aqueous synthesis of stable few-layered 1T-MoS_2 : applications for visible-light-driven photocatalytic hydrogen evolution, Small 11 (2015) 5556–5564.
[34] Y. Qi, Q. Xu, Y. Wang, B. Yan, Y. Ren, Z. Chen, CO_2-induced phase engineering: protocol for enhanced photoelectrocatalytic performance of 2D MoS_2 nanosheets, ACS Nano 10 (2016) 2903–2909.
[35] P. Zhang, C. Gao, B. Xu, L. Qi, C. Jiang, M. Gao, D. Xue, Structural phase transition effect on resistive wwitching behavior of MoS_2 -polyvinylpyrrolidone nanocomposites films for flexible memory devices, Small 12 (2016) 2077–2084.
[36] P. Mondal, A. Sinha, N. Salam, A.S. Roy, N.R. Jana, S.M. Islam, Enhanced catalytic performance by copper nanoparticle–graphene based composite, RSC Adv. 3 (2013) 5615.
[37] J.X. Feng, J.Q. Wu, Y.X. Tong, G.R. Li, Efficient hydrogen evolution on Cu nanodots-decorated Ni_3S_2 nanotubes by optimizing atomic hydrogen adsorption and desorption, J. Am. Chem. Soc. 140 (2018) 610–617.
[38] J.X. Feng, H. Xu, Y.T. Dong, X.F. Lu, Y.X. Tong, G.R. Li, Efficient hydrogen evolution electrocatalysis using cobalt nanotubes decorated with titanium dioxide nanodots, Angew. Chem. Int. Ed. Engl. 56 (2017) 2960–2964.
[39] Q. Liu, Q. Fang, W. Chu, Y. Wan, X. Li, W. Xu, M. Habib, S. Tao, Y. Zhou, D. Liu, T. Xiang, A. Khalil, X. Wu, M. Chhowalla, P.M. Ajayan, L. Song, Electron-doped 1T-MoS_2 via interface engineering for enhanced electrocatalytic hydrogen evolution, Chem. Mater. 29 (2017) 4738–4744.
[40] Y. Hong, J. Zhang, F. Huang, J. Zhang, X. Wang, Z. Wu, Z. Lin, J. Yu, Enhanced visible light photocatalytic hydrogen production activity of CuS/ZnS nanoflower spheres, J. Mater. Chem. A 3 (2015) 13913–13919.
[41] K.K. Liu, W. Zhang, Y.H. Lee, Y.C. Lin, M.T. Chang, C.Y. Su, C.S. Chang, H. Li, Y. Shi, H. Zhang, C.S. Lai, L.J. Li, Growth of large-area and highly crystalline MoS_2 thin layers on insulating substrates, Nano Lett. 12 (2012) 1538–1544.
[42] V.O. Koroteev, L.G. Bulusheva, A.V. Okotrub, N.F. Yudanov, D.V. Vyalikh, Formation of MoS_2 nanoparticles on the surface of reduced graphite oxide, Phys. Status Solidi B 248 (2011) 2740–2743.
[43] L. Liao, J. Zhu, X. Bian, L. Zhu, M.D. Scanlon, H.H. Girault, B. Liu, MoS_2 formed on mesoporous graphene as a highly active catalyst for hydrogen evolution, Adv. Funct. Mater. 23 (2013) 5326–5333.
[44] Y. Qu, H. Medina, S.W. Wang, Y.C. Wang, C.W. Chen, T.Y. Su, A. Manikandan, K. Wang, Y.C. Shih, J.W. Chang, H.C. Kuo, C.Y. Lee, S.Y. Lu, G. Shen, Z.M. Wang, Y.L. Chueh, Wafer scale phase-engineered 1T- and 2H-$MoSe_2$ /Mo core-shell 3D-hierarchical nanostructures toward efficient electrocatalytic hydrogen evolution reaction, Adv. Mater. 28 (2016) 9831–9838.
[45] Y. Fang, J. Pan, J. He, R. Luo, D. Wang, X. Che, K. Bu, W. Zhao, P. Liu, G. Mu, H. Zhang, T. Lin, F. Huang, Structure re-determination and superconductivity observation of bulk 1T MoS_2, Angew. Chem. Int. Ed. Engl. 57 (2018) 1232–1235.